 doi:10.20944/preprints202008.0150.v1

Article

Limiting the Oxidation of WS_2 Nanostructures by Oleylamine Surface Passivation for Room Temperature NH_3 Sensing

Siziwe Gqoba [1,*], Rafael Rodrigues [2], Sharon Lerato Mphahlele [1], Zakhele Ndala [1], Mildred Airo [1], Tshwarela Kolokoto [1], Ivo A. Hümmelgen [2], Ella C. Linganiso [1,3], Makwena J. Moloto [4] and Nosipho Moloto [2,*]

[1] Molecular Sciences Institute, School of Chemistry, University of the Witwatersrand, Wits, 2050, Republic of South Africa; Siziwe.gqoba@wits.ac.za (SG); leratosharonm@gmail.com (LSM); 491384@students.wits.ac.za (ZN); mildred.airo@wits.ac.za (MA); 670850@students.wits.ac.za (TK); cebisa.linganiso@wits.ac.za (CEL); nosipho.moloto@wits.ac.za (NM)

[2] Departamento de Física,Universidade Federal do Paraná, 81531-980 Curitiba, Brazil; rafael779@gmail.com (RR); iah@fisica.ufpr.br (IAH)

[3] Microscopy and Microanalysis Unit, University of the Witwatersrand, Wits, 2050, Republic of South Africa; cebisa.linganiso@wits.ac.za (ECL)

[4] Department of Chemistry, Vaal University of Technology, Vanderbijlpark, 1900, Republic of South Africa; makwenam@vut.ac.za (MJM)

* Correspondence: Siziwe.gqoba@wits.ac.za; Tel.: +27 11 717 6756 (SG); nosipho.moloto@wits.ac.za (NM); Tel.: +27-11-717-6774

Abstract: Oleylamine capped WS_2 nanostructures were successfully formed at 320 °C via a relatively simple colloidal route. SEM and TEM analyses showed that the 3D nanoflowers that were initially formed disintegrated into 2D nanosheets after prolonged incubation. XPS and XRD analyses confirmed oxidation of WS_2 into WO_3. Sensors based on these oleylamine capped WS_2 nanoflowers and nanosheets still showed a change in electrical response towards various concentrations of NH_3 vapour at room temperature in a 25% relative humidity background despite the oxidation. The nanoflowers exhibited n-type response while the nanosheets displayed a p-type response towards NH_3 exposure. The nanoflower based sensors showed better response to NH_3 vapour exposure than the nanosheets. The sensors showed a good selectivity towards NH_3 relative to acetone, ethanol, chloroform and toluene. Meanwhile, a strong interference of humidity to the NH_3 response was displayed at high relative humidity levels. The results demonstrated that oleylamine limited the extent of oxidation of WS_2 nanostructures. The superior sensing performance of the nanoflowers can be attributed to their hierarchical morphology which enhances the surface area and diffusion of the analyte.

Keywords: oleylamine; WS_2; nanoflowers; gas sensing

1. Introduction

Semiconducting 2D layered transition metal dichalcogenides (TMDCs) are among the most interesting materials for application in gas sensing devices. Their large surface area provides abundant sites for the adsorption of gas molecules. In addition, TMDCs do not require high working temperatures; unlike their oxide counterparts. Among these TMDCs is WS_2 with a tunable band gap of 1.35 − 2.1 eV [1], higher phonon-limited electron mobility and stronger thermal stability than other TMDCs [2]. Consequently, the sensing properties of various WS_2 materials (pristine and modified) to gases such as acetone, NO_2 [3, 4], NH_3 [2], humidity [5], H_2S [6], H_2 [4, 5], ethanol [7] and O_2 [7], CO

 doi:10.20944/preprints202008.0150.v1

[6], NO [6] have been reported. Among these gases is NH_3 which has found application in the chemical and fertilizer industries, explosives and medical diagnostics [2]. However, its accumulation has a very negative impact to human health and the environment.

Of the various synthetic methods employed to fabricate WS_2 nanostructures, the colloidal method provides a platform for tuning the morphology, electrical and optical properties of the nanostructures. This is achieved by merely varying reaction conditions such as the choice of precursors, concentration, capping agents, time and temperature [8-10]. Different morphologies of WS_2 nanostructures such as nanorods, nanoflakes, nanoflowers and nanosheets have been fabricated through these synthetic methods for application in gas sensing. The gas sensing performance of nanosheets and nanoflakes of pristine and functionalized WS_2 is well documented [2-6]. However, the unusual geometry and robust structure of the nanoflower morphology is generating a considerable amount of curiosity. Nanoflowers, whose building blocks are nanorods/well-ordered needles (1D) and sheets/plate-like petals (2D) [11]; are highly desirable materials in gas sensing given the larger surface area and increased available interspace they possess [12]. Their impressive properties are attributed to the advantages provided by both their nanometre-sized building blocks and their overall micrometer-sized structure [12]. As such, nanoflowers have been applied in photocatalysis [13], energy storage [14] and hydrogen energy generation with reports of enhanced performance [15]. Therefore, application of WS_2 nanoflowers in gas sensors warrants investigation.

It is worthy to note that WS_2 is very unstable in air and undergoes oxidation to form amorphous WO_3. Furthermore, large amounts of WO_3 on the surface of WS_2 hamper its room temperature (RT) sensitivity towards NH_3. To that effect, strategies such as the formation of a large organic shell around the nanoparticles have been developed to prevent complete oxidation [16]. Perozzi and co-workers demonstrated that partially oxidized WS_2 nanoflakes were still sensitive to NH_3 at an operating temperature of 150 °C [4].

Humidity interference is highly prevalent in RT gas sensing due to the ease of adsorption of the dense and highly electronegative water molecules on the surface of the sensor. This produces an electrical response, resulting in increased or decreased response of the sensor to the target analyte. Li et al. reported an increase in the response of WS_2 nanoflakes based sensors to NH_3 at RT due to an increase in humidity [17]. However, this increase was reportedly observable up to 73% relative humidity (RH).

Herein, the formation of nanoflowers of oleylamine (OLA) capped WS_2 (OLA/WS_2) is outlined. The nanoflowers were fabricated using a simple, colloidal method (320 °C) with OLA as the solvent. OLA also played the role of an organic shell; capping the particles thereby partially protecting the core WS_2 from oxidation. Prolonged heating of the reaction mixture resulted in the disintegration of the 3D hierarchical nanoflowers into 2D nanosheets. Furthermore, the RT gas sensing performance and mechanism of the OLA/WS_2 nanoflowers and nanosheets towards NH_3 are documented. The selectivity of the OLA/WS_2 sensors to some of the common interferents and the effect of background humidity towards NH_3 response are also reported.

2. Materials and Methods

2.1 Chemicals

Tungstic acid (H_2WO_4), thiourea ($CS(NH_2)_2$), oleylamine (OLA), ammonium hydroxide NH_4OH, ethanol (CH_3CH_2OH), hexane (C_6H_{14}), chloroform ($CHCl_3$), toluene ($C_6H_5CH_3$), acetone ($(CH_3)_2CO$), isopropyl alcohol (C_3H_8O) were all of analytical grade and were used as received.

2.2 Synthesis of OLA/WS_2 nanostructures

A 1:4 ratio of H_2WO_4 to $CS(NH_2)_2$ was used. OLA (20 mL) was heated at RT with continuous stirring under N_2 gas flow for 15 min in a three-neck round bottom flask. Crystalline $CS(NH_2)_2$ (1.6016 g) and H_2WO_4 (1.2492 g) were added to the mixture; and heated rapidly to 320 °C to allow for the

 doi:10.20944/preprints202008.0150.v1

decomposition of both precursors. Several colour changes were observed during the reaction process indicating the formation of intermediates (Figure S1). Ultimately, the mixture turned thick black pointing to the formation of WS_2 nanostructures. The reaction was held at 320 °C for 15 min to allow for growth of nanostructures. Subsequent aliquots of the black product were taken at 15, 45, 60, 180 and 240 min. Separation of the colloids from the growth solution was effected by the addition of ethanol after cooling the samples for 5 min. Centrifugation was used to collect the nanostructures while an ethanol/hexane (1:1) was used to remove excess OLA. The resulting black powders were dried RT and re-dispersed in chloroform for further characterization.

2.3 Materials characterization

2.3.1 Optical characterization

Absorption measurements were carried out using a Specord 50 Analytik Jena UV-vis spectrophotometer. An Agilent Cary Eclipse fluorescence spectrometer was used to measure the photoluminescence (PL) of the particles. Estimated of the number of the nanostructure layers was through Raman spectroscopy (Bruker Senterra Infinity 1 software, 50 X optical objective, 532 nm laser wavelength, 0.2 mV laser power and integration power of 15 s). The nanoparticles were used as dry powders for Raman spectroscopy, while they were dissolved in $CHCl_3$ and placed in quartz cuvettes (1cm path length) for UV-vis absorption and PL spectral analyses.

2.3.2 Structural characterization

The structure and phase of the powdered nanomaterials were determined with the Bruker MeasSrv (D2-205530)/D2-205530 diffractometer using secondary graphite monochromated CuKα radiation (λ 1.54060 Å) at 30 kV/30 mA. Measurements were taken using a glancing angle of incidence detector at an angle of 2°, for 2θ values over 10 - 90° in steps of 0.026° with a step time of 37 s and at a temperature of 25 °C. The surface properties were determined using X-ray photoelectron spectroscopy measurements which were performed with a PHI 5000 Versaprobe - Scanning ESCA Microprobe operating with a 100 μm 25 W 15 kV Al monochromatic X-ray beam. Sizes and morphologies of the nanomaterials were studied using a FEI Nova NanoLab FIB/SEM and a JEOL JEM-2100 field emission gun transmission electron microscope, operated at 200 kV. Chemical composition of the crystal structure was analysed with energy-dispersive x-ray spectroscopy (EDS).

2.4 Gas sensing performance measurements

2.4.1 Device fabrication

Sensor devices were prepared using interdigitated electrodes (IDEs) of electroless nickel immersion gold (ENIG) patterned onto FR4 epoxy resin/fibre glass substrate, which were purchased from Micropress SA. These electrodes consist of 18 pairs of 7.9 mm long stripes with a gap of 0.1 mm between them, occupying 57 mm^2 of active area. The electrodes were cleaned with acetone, deionized water and isopropyl alcohol sequentially in a 135 W ultrasonic bath for 20 min each. In sequence, the electrodes were dried in an oven at 100 °C for 30 min and finally placed in a UV ozone cleaner (Novascan; intense 185 nm and 254 nm ultraviolet light) for 30 min in order to remove organic residues. OLA/WS_2 dispersions were prepared in toluene at a concentration of 5 mg/mL. The dispersion was ultra-sonicated at room temperature for 30 min before deposition of 20 μL onto the cleaned IDEs. The sensors were kept in an oven for 30 min at 130 °C, in order to evaporate the solvent. The final thickness of the sensors was determined with a surface profiler (Dektak XT; Bruker) and was found to be about 600 nm for all samples.

2.4.2 Gas sensing set-up

The OLA/WS_2 based sensors were placed in the in-house custom made testing equipment depicted by Figure 1. The system was purged with dry nitrogen N_2 for 15 min to reduce RH to 25%,

 doi:10.20944/preprints202008.0150.v1

providing a controlled atmosphere. The chamber was grounded and 1 h stabilization period in dry N_2 was performed before starting the electrical measurements. Electrical measurements were performed in the dark, using a LCR meter (Agilent 4284A 20 Hz – 1 MHz Precision LCR meter) attached to a computer interfaced with a GPIB for data acquisition. An operational voltage and frequency of 1000 mV and 10 kHz were selected respectively.

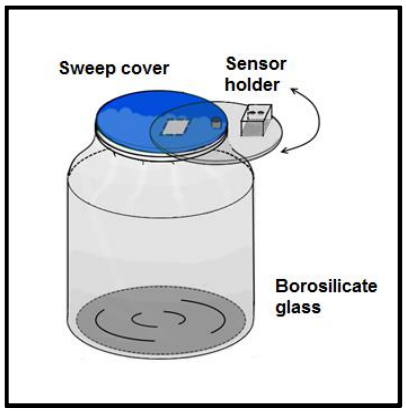

Figure 1. Schematic representation of the gas chamber used for sensor measurements.

2.4.3 Sensitivity of OLA/WS_2 sensors to NH_3 at 25% RH

The electrical conductance measurements of sensors based on OLA/WS_2 nanostructures were performed with incremental NH_3 concentrations at RT (~ 23 °C) and 25% RH. Each measurement was characterized by a 50 s stabilizing period followed by introduction of 1.5 µL of NH_4OH (analyte) at every 200 s into the chamber depicted by Figure 1. The time interval was enough to evaporate the analyte and saturate the chamber. The measurements were done with concentrations of NH_4OH in the range of 240 - 958 ppm.

2.4.4 Sensitivity of OLA/WS_2 sensor (45 min) to NH_3 at various RH

Humidity interference was investigated by introducing the sensors to incremental concentrations of NH_3 at different RH conditions. The humidity levels were obtained by introducing different saturated salt solutions into the chamber at RT. The saturated solutions of KOH, $MgCl_2$, NaBr, NaCl and K_2SO_4 were prepared following the procedure outlined by Greenspan [18] to obtain 41, 69, 75, 87 and 97% RH. The chamber depicted by Figure 1 was used.

2.4.5 Selectivity of OLA/WS_2 sensor (45 min) to interferents at 25% RH

Specificity of the sensor was determined by subjecting it to volatile organic compounds (VOCs) such as acetone, chloroform, ethanol and toluene. Each measurement was characterized by a 50 s stabilizing period followed by introduction of 1.5 µL of the interferent at every 200 s into the chamber depicted by Figure 1. The time interval was enough to evaporate the VOCs and saturate the chamber. The measurements were done with incremental concentrations of each interferent.

2.4.6 Sensor response-recovery curves

The measurements were performed at ambient conditions for all the sensors using the chamber in Figure 1. The chamber was saturated with NH_3.

3. Results and discussion

Preprints (www.preprints.org) | NOT PEER-REVIEWED | Posted: 6 August 2020 doi:10.20944/preprints202008.0150.v1

3.1. Proposed reaction mechanism

The synthesis of OLA/WS_2 nanostructures involves the formation of intermediates based on the observations made during the synthesis and those reported in literature [19]. Herein, H_2WO_4 decomposed at approximately 120 °C into tungsten trioxide (WO_3) and steam. Meanwhile, thiourea decomposed between 180 and 200 °C into carbon disulphide (CS_2), cyanamide (H_2NCN) and NH_3 gases. WO_3 (W^{6+}) was later sulfurized by carbon disulphide into WS_2 (W^{4+}). The proposed reaction mechanism is expressed below:

$$H_2WO_4\,(s) \xrightarrow[N_2,\ 320\ ^\circ C]{OLA} WO_3\,(s) + H_2O\,(g) \quad (1)$$

$$2CS(NH_2)_2\,(s) \xrightarrow[N_2,\ 320\ ^\circ C]{OLA} CS_2\,(g) + H_2NCN + 2NH_3\,(g) \quad (2)$$

$$2WO_3 + 3CS_2\,(g) \xrightarrow[N_2,\ 320\ ^\circ C]{OLA} 2WS_2 + 3CO_2\,(g) + 2S \quad (3)$$

3.2. Characterization of OLA/WS_2 nanostructures

The morphologies of the as synthesized particles were determined by SEM. Shown in Figure 2 are the SEM micrographs of OLA/WS_2 nanostructures synthesized at different reaction times. Round shaped nanoflowers of ≈ 375 nm were formed at a growth time of 15 min. An increase in the reaction time to 45 min led to open shaped nanoflowers with a slight increase in diameter of ≈ 400 nm. The circled nanoflower shows how the petals are interconnected thus providing more sites for surface reactions e.g. adsorption of gas molecules. After 60 min of incubation, the nanoflowers started to disintegrate forming curled edges as shown by the red circle. The curling is due to the instability of the nanopetals with the tendency to form a closed structure by rolling up. This reduces dangling bonds and the total energy of the system. When the reaction time was increased to 180 min, individual nanosheets were formed. This suggests that the nanoflowers were assembled from nanosheets. The nanosheets may have formed under 15 min.

Preprints (www.preprints.org) | NOT PEER-REVIEWED | Posted: 6 August 2020 doi:10.20944/preprints202008.0150.v1

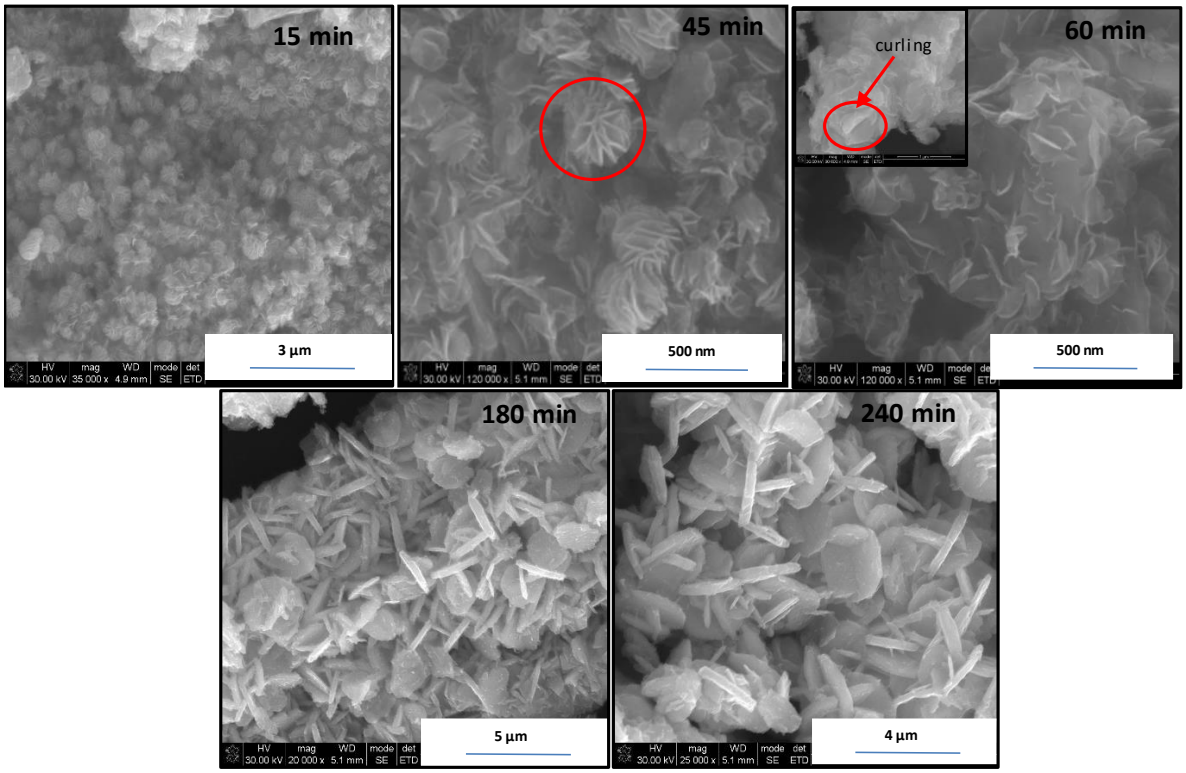

Figure 2. SEM micrographs of OLA/WS_2 nanostructures at different reaction times.

To further understand the morphology of the OLA/WS_2 nanostructures, TEM studies of the samples were undertaken, Figure 3. A 15 min incubation produced densely packed fluffy-like spherical particles. These correspond to the round shaped nanoflowers obtained at 15 min in the SEM micrograph (Figure 2). After 45 min of heating, open nanoflowers were observed as shown on the inset; in agreement with SEM analysis. As the time was prolonged to 60 min, nanosheets appeared and seemed crumpled at some of the edges. This observation is consistent with the rolling/curling of the nanosheets in the SEM micrograph, Figure 2. Fine hair-like strands were observed with further incubation at 180 and 240 min, suggesting a similar kind of morphology at both reaction times. This too is in agreement with the SEM micrographs where nanosheets were observed at both reaction times.

Preprints (www.preprints.org) | NOT PEER-REVIEWED | Posted: 6 August 2020 doi:10.20944/preprints202008.0150.v1

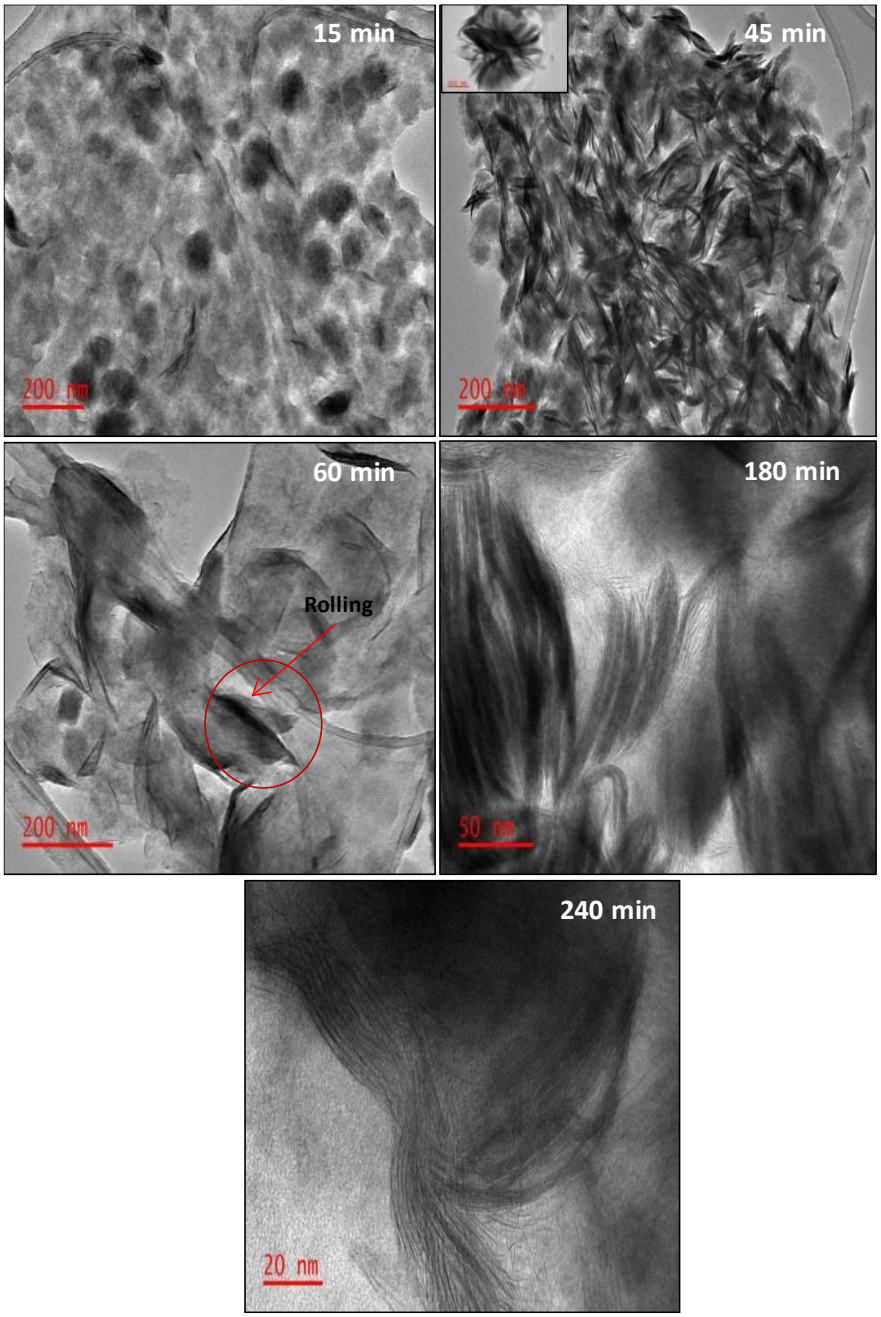

Figure 3. TEM micrographs of OLA/WS_2 nanocrystals synthesized at different times.

The change in morphology of OLA/WS_2 nanostructures is summarized in Figure 4.

Preprints (www.preprints.org) | NOT PEER-REVIEWED | Posted: 6 August 2020 doi:10.20944/preprints202008.0150.v1

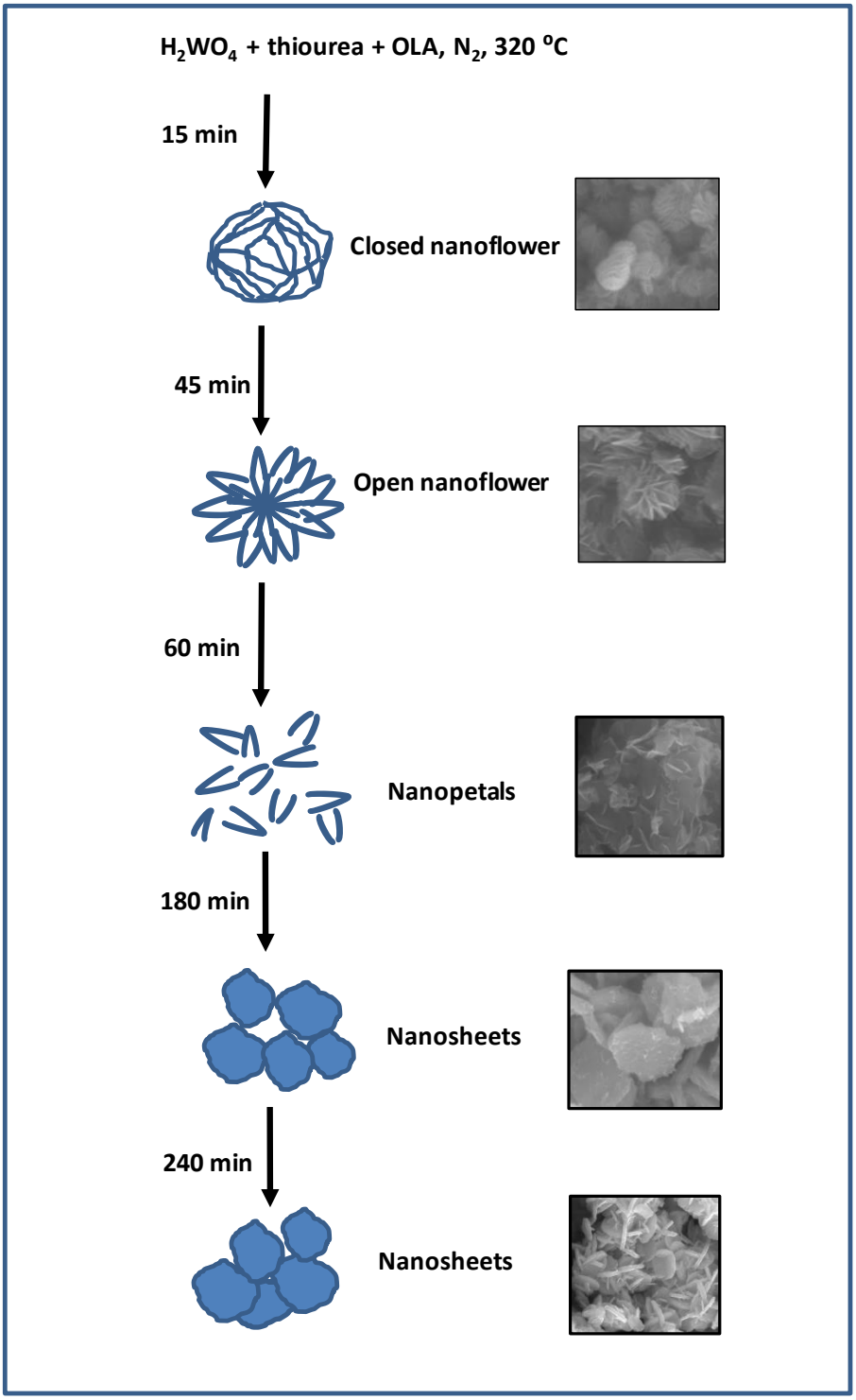

Figure 4. A schematic illustration of the change in morphology of OLA/WS_2 nanoflower to nanosheets as a function of time.

EDS analysis confirmed the presence of W and S (Figure S2).

The nanostructures were further characterized with X-ray diffraction to confirm the crystal phase and purity of OLA/WS_2. XRD patterns of the nanostructures synthesized at different times are shown in Figure 5. All the diffraction patterns are indexed to the 2H-WS_2 polytype according to PDF No: 00-002-0131\JCP2.2CA. The samples show good crystallinity. The broadness and prominence of

Preprints (www.preprints.org) | NOT PEER-REVIEWED | Posted: 6 August 2020 doi:10.20944/preprints202008.0150.v1

the (002) peak in all the samples suggests reduced size of the nanostructures as well as the existence of more than one layer of sheets. A small peak for was observed for both 15 min and 45 min samples and is associated with WO_3 at 29.5°. The intensity of the peak suggests partial oxidation, indicating that WO_3 does not make up the bulk of the sample. The peak however disappears as the time is prolonged. The presence of the (002) peak in the XRD is usually used as an indicator of the number of layers present with its prominence suggesting multiple layers.

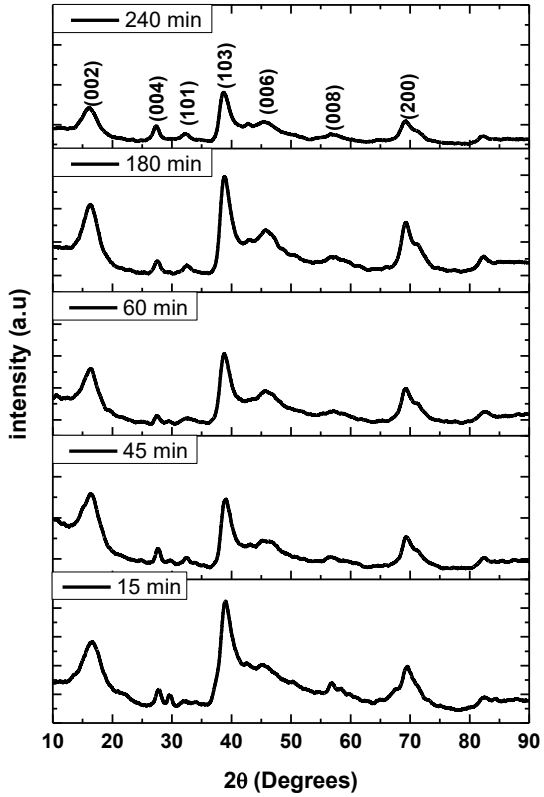

Figure 5. X-ray diffraction patterns of OLA/WS_2 synthesized at different reaction times.

The structure of layered materials was further characterized by Raman spectroscopy; thereby estimating the number of the layers. Figure 6 shows the Raman spectra of the as-synthesized OLA/WS_2 nanostructures. Two prominent peaks are observed which are characteristic of the second order longitudinal acoustic 2LA(M) at approximately 350 cm^{-1} and out-of-plane $A_{1g}(\Gamma)$ at approximately 415 cm^{-1} for all samples. In addition, a shoulder peak at 313 cm^{-1} belonging to an in-plane $E_{12g}(\Gamma)$ is also observed. There is a slight shift to lower frequencies from bulk for both $A_{1g}(\Gamma)$ and 2LA(M) (356 and 421 cm^{-1} for bulk respectively) associated with decreasing interlayer interactions by van der Waals forces suggesting the formation of a few layers or monolayers. This is in agreement with results obtained by Varghese *et al*. [20] and Tan *et al*. for bi-layers [21]. The intensities of the 2LA(M) are slightly higher than that of $A_{1g}(\Gamma)$ and the ratios are depicted in Table S1. According to Berkdemir and co-workers, the values suggest the formation of bi-layers [22]. It has been reported that the number of layers is indirectly proportional to the intensity of 2LA(M) mode and vice-versa for $A_{1g}(\Gamma)$ [23]. So, 2LA(M) should have an intensity almost twice that of $A_{1g}(\Gamma)$ for a monolayer. Herein, the intensity of 2LA(M) is not twice that of $A_{1g}(\Gamma)$, but still higher, thus suggesting a bi-layer. Furthermore, the frequency difference can also be used as an indication of the number of layers and the values depicted in Table S1 also suggest the formation of bi-layers. Therefore, the existence of a few layers is plausible based on the morphologies observed in Figure 2.

 doi:10.20944/preprints202008.0150.v1

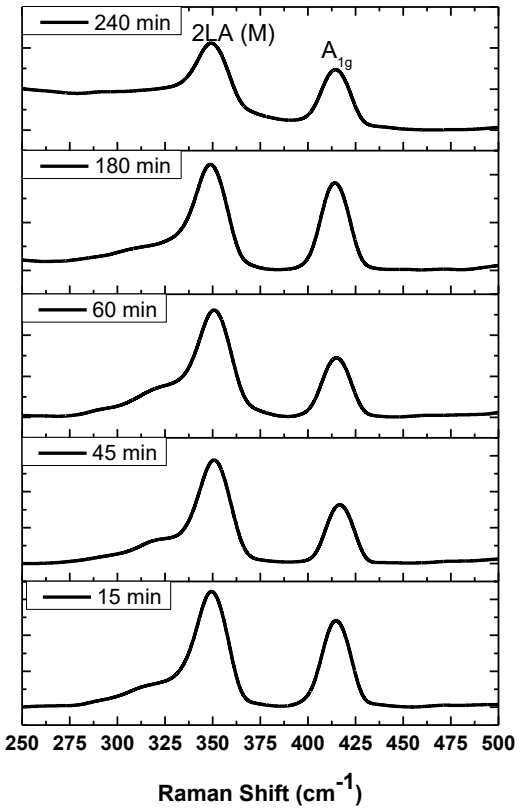

Figure 6. Raman spectra of OLA/WS_2 synthesized at different reaction times.

To establish the extent of oxidation to WO_3, XPS studies were done. The survey spectrum of the nanostructures obtained in 45 min is shown in Figure 7. Identical results were obtained for all the other samples; hence they will not be discussed. The spectrum showed a strong C 1s peak confirming the presence of carbon due to the capping agent, OLA on the surface of the nanocrystals. The presence of the carbon peak is attributed to the capping agent; this is consistent with other published work on capped nanoparticles. XPS has been used previously to trace ligand exchange on the surface of the nanocrystals [24, 25]. The oxygen is due to both the presence of WO_3 and the oxidation of the capping agent. Also, observed are the W and S peaks as a result of WS_2 and WO_3. The atomic % composition and peak area % are shown in Table 1. The sample was found to be largely made up of carbon, of which 77.4% of it was attributed to the capping agent that forms a large organic shell around each particle.

Preprints (www.preprints.org) | NOT PEER-REVIEWED | Posted: 6 August 2020 doi:10.20944/preprints202008.0150.v1

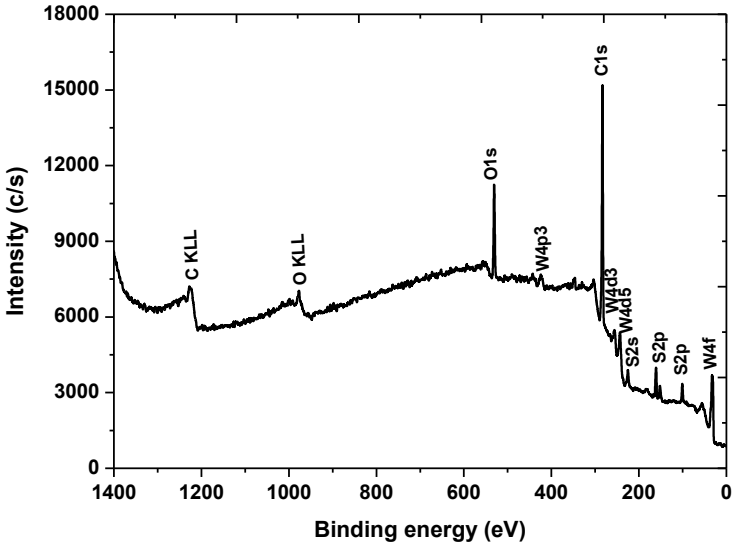

Figure 7. XPS survey spectrum of OLA/WS_2 synthesized in 45 min.

Table 1. Summary of the atomic composition stoichiometric assignments obtained from the fitting of the XPS spectra of OLA/WS_2.

Element	Atomic %	Peak Binding energy (eV)	Assignments	Peak area %
C	77.4	284.8	C-C	91
		286.3	C-O	6
		288.9	O-C=O	3
O	10.8	532.2	C-O	100
W	3.7	30.9	WS_2	41
		33.2	WS_2	38
		34.4	W^{5+}	6
		36.3	WO_3	15
S	6.2	159.5	S_2W def.	9
		160.6	S_2W	60
		161.8	S_2W	31

Preprints (www.preprints.org) | NOT PEER-REVIEWED | Posted: 6 August 2020 doi:10.20944/preprints202008.0150.v1

In Figure 8, the C 1s core level spectrum shows the deconvoluted C-C peak which is due to OLA; Meanwhile, the C-O and O-C=O were attributed to the oxidation of OLA. The O 1s peak also shows the oxidation of the capping agent. The W_{4f} core level spectrum comprises of four components; the W $4f_{7/2}$ (30.9 eV), the W $4f_{5/2}$ (33.2 eV) doublet, the W $5p_{3/2}$ (34.4 eV) and WO_3 (36.3 eV). The W $4f_{7/2}$ and W $4f_{5/2}$ are ascribed to the 2H-WS_2 polytype, the W $5p_{3/2}$ is attributed to the partially coordinated W in WO_3 whilst WO_3 is fully coordinated W [4]. The S 2p core level spectrum shows three peaks all attributed to the semiconducting 2H-WS_2 polytype. The W 4f component shows 21% total abundance of WO_3 and 79% abundance of WS_2. These results are similar to other reported work where it has been proven that partial oxidation of WS_2 does not adversely affect the sensing of NH_3 [4]. Moreover, the surface defects (W^{5+} and defect S_2W) provide additional active sites for the adsorption of gas molecules; thereby enhancing the response [4].

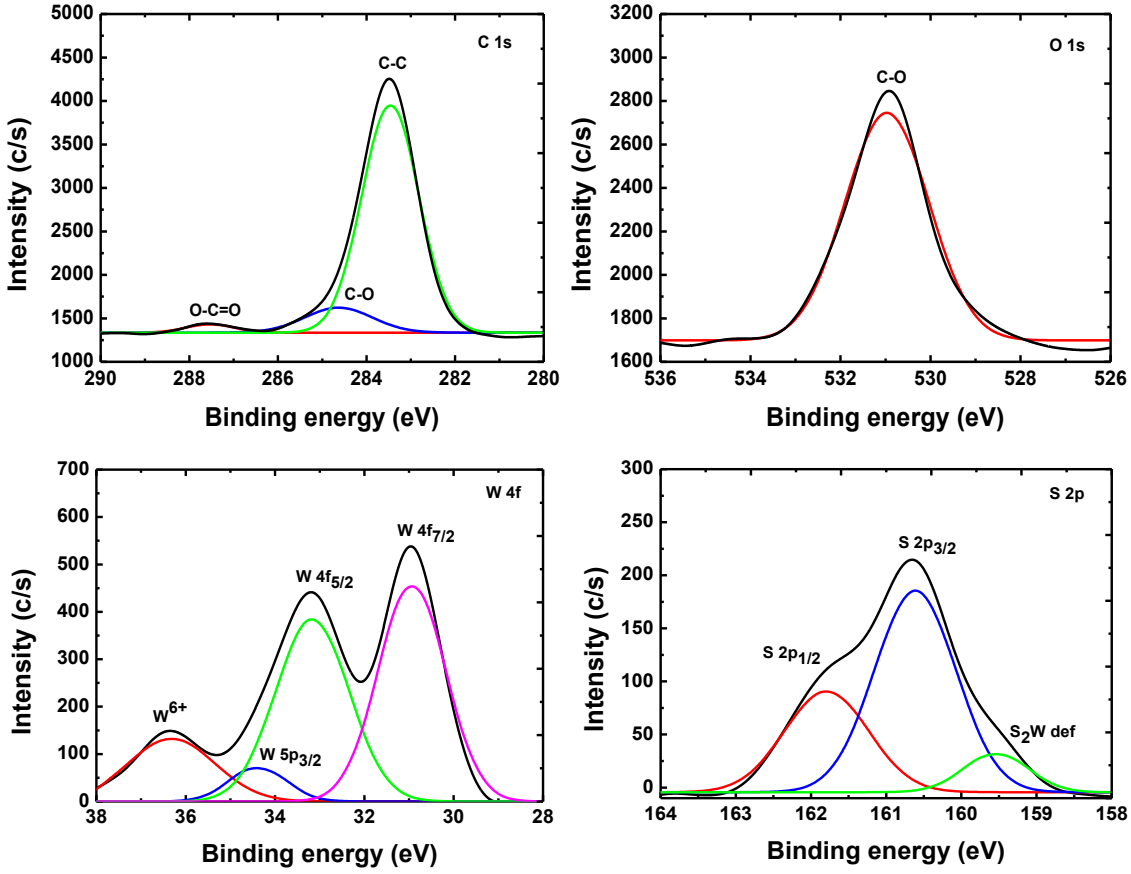

Figure 8. High resolution core level spectra of OLA/WS_2 with focus on C 1s, O 1s, W 4f and S 2p.

The presence of the capping agent on the surface of WS_2 was further confirmed by FT-IR spectroscopy (Figure S3).

UV-vis absorption and photoluminescence spectroscopy were used to determine the optical properties of the as-synthesized OLA/WS_2 nanostructures. Figure 9 (a) shows the UV-vis absorption spectra with characteristic absorption peaks similar to results obtained by Cao *et al*. [26]. The results for all samples are summarized in Table S2. The blue shifted 625 - 630 nm and 505 -515 nm peaks correspond with excitons A and B (636 and 525 nm for bulk WS_2 respectively) [27] (inset). Meanwhile, C and D are due to the direct transitions from the valence band to the conduction band (inset). Bulk WS_2 has an indirect band gap of 1.3 -1.4 eV and crosses over to the direct band gap of 1.9 - 2.05 eV

Preprints (www.preprints.org) | NOT PEER-REVIEWED | Posted: 6 August 2020 doi:10.20944/preprints202008.0150.v1

when thinned to monolayer [28]. The band gap values for all samples correspond to the exciton 'A' (1.96 - 198 eV) thereby confirming the crossover.

The PL spectra for all samples are shown in Figure 9 (b). Broad photoluminescence peaks stretching from 675 - 790 nm are observed. The diminished PL intensity also points to the existence of more than one layer. A monolayer has a strong PL signal. However, in this case, the intensity of the PL decreased with an increase in the number of layers. Gutiérrez *et al*. suggested the weak PL of bi- layers were a result of a competition between the indirect transitions at the local minimum of conduction at the T point; and the local maximum of valence band at Γ point with the direct transitions at K point [29].

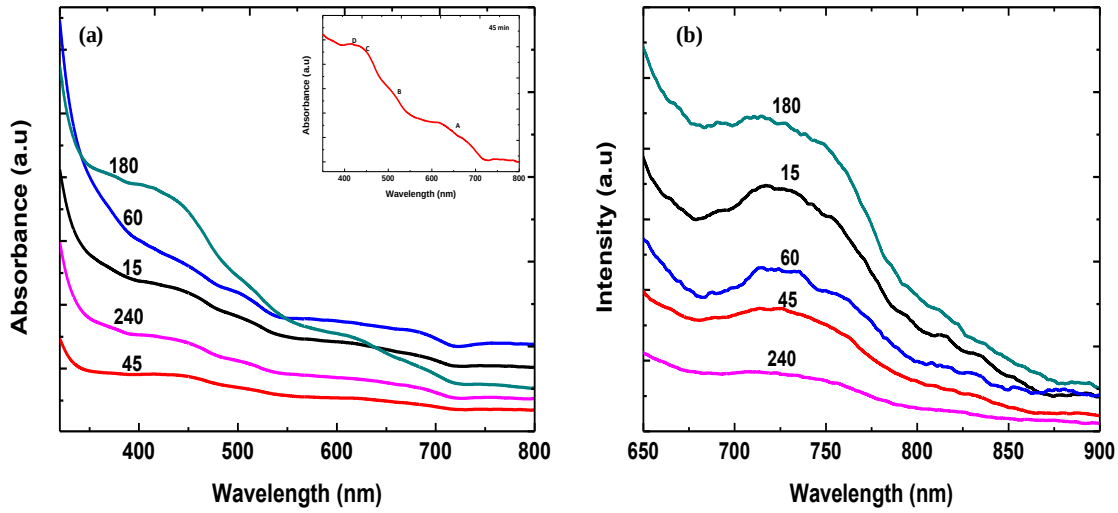

Figure 9. (a) UV-vis absorption, and (b) photoluminescence spectra of OLA/WS_2 synthesized at different reaction times.

3.3. Gas sensing performance

3.3.1. Sensitivity of the OLA/WS_2 based sensors

Figure 10 shows the sensitivities of OLA/WS_2 based sensors to different concentrations of NH_3. The gas responses of sensors were investigated with incremental increases of NH_3 concentration (240 to 958 ppm). The sensitivity of each sensor to NH_3 vapour was calculated as follows:

$$S = \frac{\partial\left(\Delta G/G_0\right)}{\partial C}, \quad (4)$$

where, S is the sensitivity in ppm^{-1}, $\Delta G/G_0$ is the relative variation of the conductance and c is the analyte concentration in ppm. The conductivity of all the OLA/WS_2 sensors changed dramatically upon exposure to NH_3 due to changes to the carrier concentration. The response is linearly proportional to the NH_3 concentration. The 15, 45 and 60 min OLA/WS_2 based sensors presented a fast response in the opposite direction (negative sensitivity) as shown in Figure 10. NH_3 is a Lewis base and therefore serves as an electron donor.

The reduction in the electrical conductance suggests that positive holes are the main charge carriers on OLA/WS_2 surface, hence the p-type doping behaviour. This is a result of depletion of

 doi:10.20944/preprints202008.0150.v1

positive (hole) charge carriers on the sensor surface by the negative charge carriers from the gas molecules. Similar behaviour was observed by Ouyang and co-workers with WS_2 nanosheets modified by Pt QDs, Li *et al.* with WS_2 nanoflakes; and Kim *et al.* with two- and five- layer MoS_2 FETs [2, 17, 30]. WS_2 has a strong Lewis acid surface that is strongly attracted to NH_3, a Lewis base [31]. Of the three sensors (15, 45 and 60 min), the 45 min derived OLA/WS_2 displayed the highest negative sensitivity followed by 15 and 60 min (sensitivities for all reaction times are summarized in Table S3). At 45 min, the petals are open, thereby providing more voids and reactive sites for gas sensing (Figure 2). The surface area is maximized for surface reactions due to the exposure of both sides of the petal for interaction with NH_3**.** Meanwhile, at 15 min the petals of the nanoflowers are still closed leading to minimal exposure of sites for interaction with NH_3. At 60 min, the nanoflowers started disintegrating leading to the loss of the nanoflower hierarchical morphology. This means the absence of voids resulting into reduced surface area which is linked to the reduced gas sensing performance. This suggests a morphology dependent sensor performance. The gas sensing performance of hierarchical structures of metal oxide (MOS) based sensors is well documented with fast and increased gas response due to the high surface area and well-defined pore framework which are ideal properties for gas sensing [32]. The surface area enhances the relative response to the analyte while the response and recovery times are influenced by the pores which favour the diffusion of the gas in and out of the sensor [33].

Morphology dependent gas sensing behaviour was also observed by Li *et al*. where cone-shaped hierarchical structures of SnO_2 annealed at 500 °C exhibited the highest relative response compared to other morphologies that were tested [33]. Meanwhile, the response of the 180 and 240 min OLA/WS_2 sensor to NH_3 was slow. Interestingly, NH_3 induced n-type doping on the 180 and 240 min OLA/WS_2 sensor as seen from the increase in conductivity (Figure 10). The main charge carriers are electrons in this case, hence the increase in conductance upon exposure to NH_3. Individual nanosheets were observed at 180 min and 240 min. The sensitivity values are overall low; this can be attributed to the presence of the capping agent on the surface of the nanostructures and/or the partial oxidation as shown by XPS (Figure 5 and 8) and FT-IR (Figure S3) results. The capping of nanostructures is necessary in colloidal synthesis to passivate the surface thus preventing agglomeration and rapid oxidation. Only trace amounts of WO_3 were detected by XPS; providing proof that OLA successfully slowed down the oxidation process. The partial oxidation was further confirmed by the sensors' response to NH_3 exposure at RT.

Preprints (www.preprints.org) | NOT PEER-REVIEWED | Posted: 6 August 2020 doi:10.20944/preprints202008.0150.v1

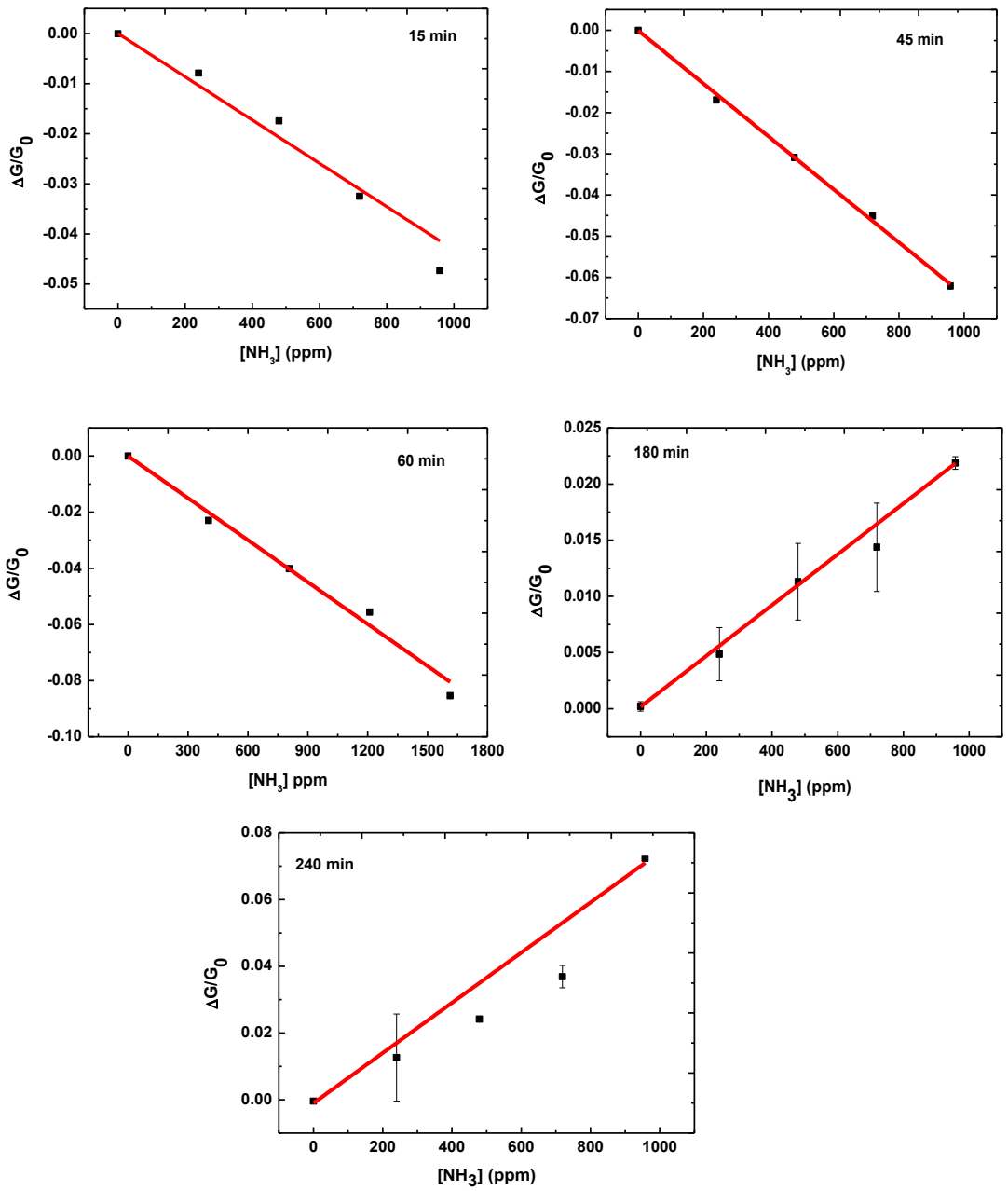

Figure 10. Sensitivity of the different OLA/WS_2 sensors to NH_3 concentrations ranging from 240 to 958 ppm. The solid red line represents the linear fit to the experimental data (black dots).

3.3.2. Specificity of the OLA/WS_2 (45 min) to selected VOCs at 25% RH

Measurements were performed on the 45 min derived sensor only because it presented the best gas sensing performance than the other four sensors. Figure 11 below shows the sensitivity of the sensor to possible interferents such as acetone, chloroform and ethanol was investigated with 25 % RH in the background.

Preprints (www.preprints.org) | NOT PEER-REVIEWED | Posted: 6 August 2020 doi:10.20944/preprints202008.0150.v1

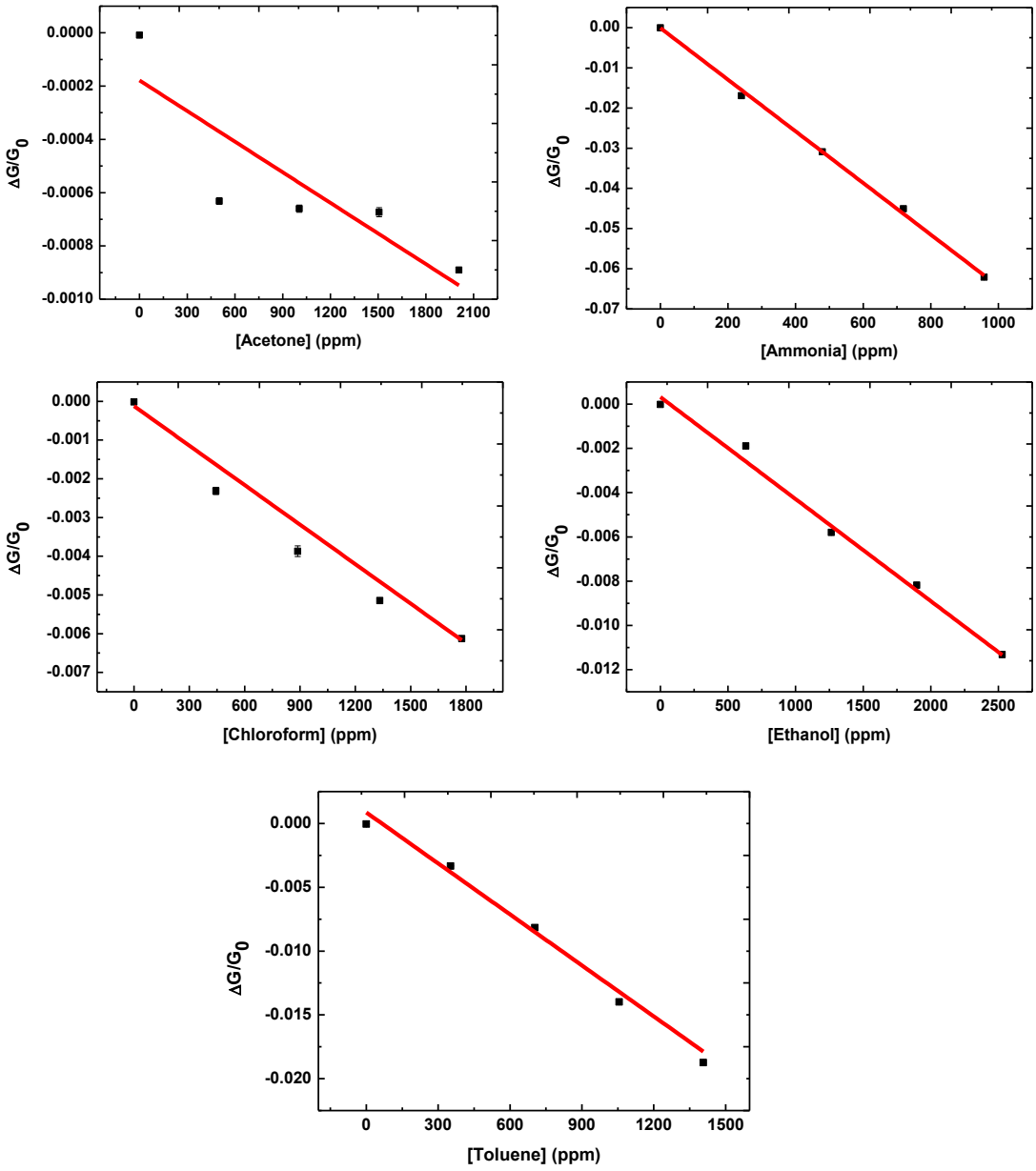

Figure 11. Sensitivity of the OLA/WS_2 sensor (45 min) to different analytes. The solid red line represents the linear fit to the experimental data (black dots).

The selectivity was determined by using the response from the calibration curves in Figure 11 and equation 5. For a sensor, considering the different analytes, the specificity (δ) to chemical species can be defined as:

$$\boldsymbol{\delta_i} = \frac{\left(\Delta G/G_0\right)_i}{\sum_{j=1}^{n}\left(\Delta G/G_0\right)_j}, \quad (5)$$

This equation was adapted from Llobet *et al.* [34]. Specificity value for the sensors can change in a range between 0 and 1. A value close to 1 is considered as representing the selective device for the target analyte relative to the interferents. The sensor displayed excellent specificity towards NH_3 over interferents as shown in Figure 12. This is probably due to the high polarity and capability of NH_3 to donate electrons to the surface molecules of the sensor. These results are in agreement with findings

Preprints (www.preprints.org) | NOT PEER-REVIEWED | Posted: 6 August 2020 doi:10.20944/preprints202008.0150.v1

by different researchers about the selectivity of various WS_2 sensors to interferents [2, 17, 31, 35]. The specificity values for each analyte are summarized in Table S4.

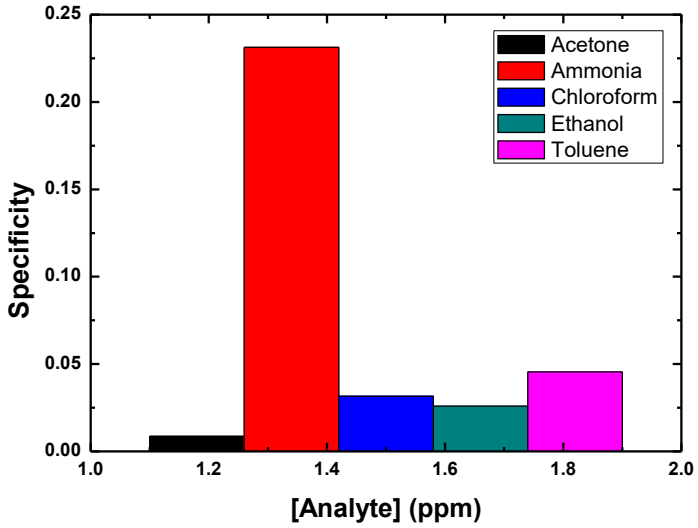

Figure 12. Specificity of the 45 min derived OLA/WS_2 sensor to 1.5 μL of each analyte at 25% RH.

3.3.3. Sensitivity of OLA/WS_2 (45 min) under different RH conditions

The effect of humidity on sensitivity of the 45 min sensor to NH_3 response was studied. Figure 13 (a) – (d) represent the sensing characteristics of the 45 min derived OLA/WS_2 sensor to various humidity conditions when exposed to 240 ppm increments of NH_3 vapour. Fluctuations in response to 240 ppm of NH_3 from 25 - 75% RH made it impossible to establish a trend, Figure 13 (a). Nonetheless, a clearer picture was painted at higher concentrations of NH_3. The observed response generally increased gradually as the humidity increased up to 75% RH. Meanwhile, a drastic increase in response to NH_3 was observed at 97% RH. This is contrary to the results obtained by Li *et al*. [17] where no further increase to NH_3 response was observed for WS_2 nanoflakes beyond 73% RH. It is obvious that the cross-sensitivity between NH_3 and humidity is significant at higher % RH levels. An increased response with increased concentrations of NH_3 under different relative humidity conditions by WS_2 nanoflakes were also reported previously [17].

Preprints (www.preprints.org) | NOT PEER-REVIEWED | Posted: 6 August 2020 doi:10.20944/preprints202008.0150.v1

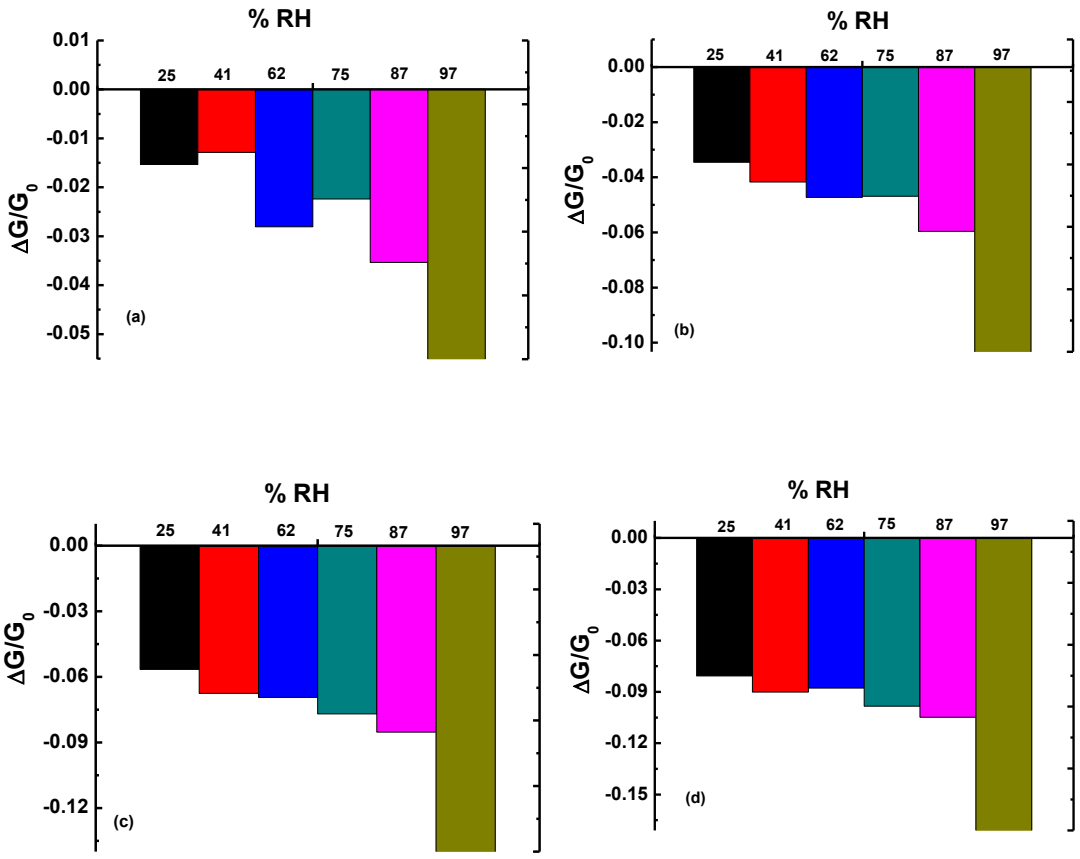

Figure 13. Histograms representing the response of OLA/WS_2 sensor (45 min) towards (a) 240 ppm, (b) 479 ppm, (c) 719 ppm and (d) 958 ppm of NH_3 under various RH conditions.

3.3.4. Response-recovery curves of OLA/WS_2 at ambient conditions

Figure 14 shows the response/recovery curves of OLA/WS_2 sensors (15, 45, 60, 180 and 240 min) obtained at ambient conditions. The characteristic sensor curve (dynamic range) was analysed and used to estimate the response and recovery times for a certain concentration of NH_3. The conductance of all the sensors decreased sharply when exposed to NH_3 giving a negative response and recovered slowly when removed from NH_3. It took the OLA/WS_2 based sensors about 28 s to show 90% change in the original conductance value. After a standing time of 300 s, the sensors were again exposed to ambient and the recovery time was measured to be about 42 s. Such slow recovery performance at RT is common to TMDC thin films based NH_3 sensors such as graphene and MoS_2 [35, 36]. The strong interactions between NH_3 molecules and the active layer were previously reported as the reason behind analyte accumulation on the surface of the sensor [37]. However, placing the device under UV light for 60 min or in an oven for 10 min at 100 °C promoted the release of NH_3 molecules and the baseline value was "reset".

Preprints (www.preprints.org) | NOT PEER-REVIEWED | Posted: 6 August 2020 doi:10.20944/preprints202008.0150.v1

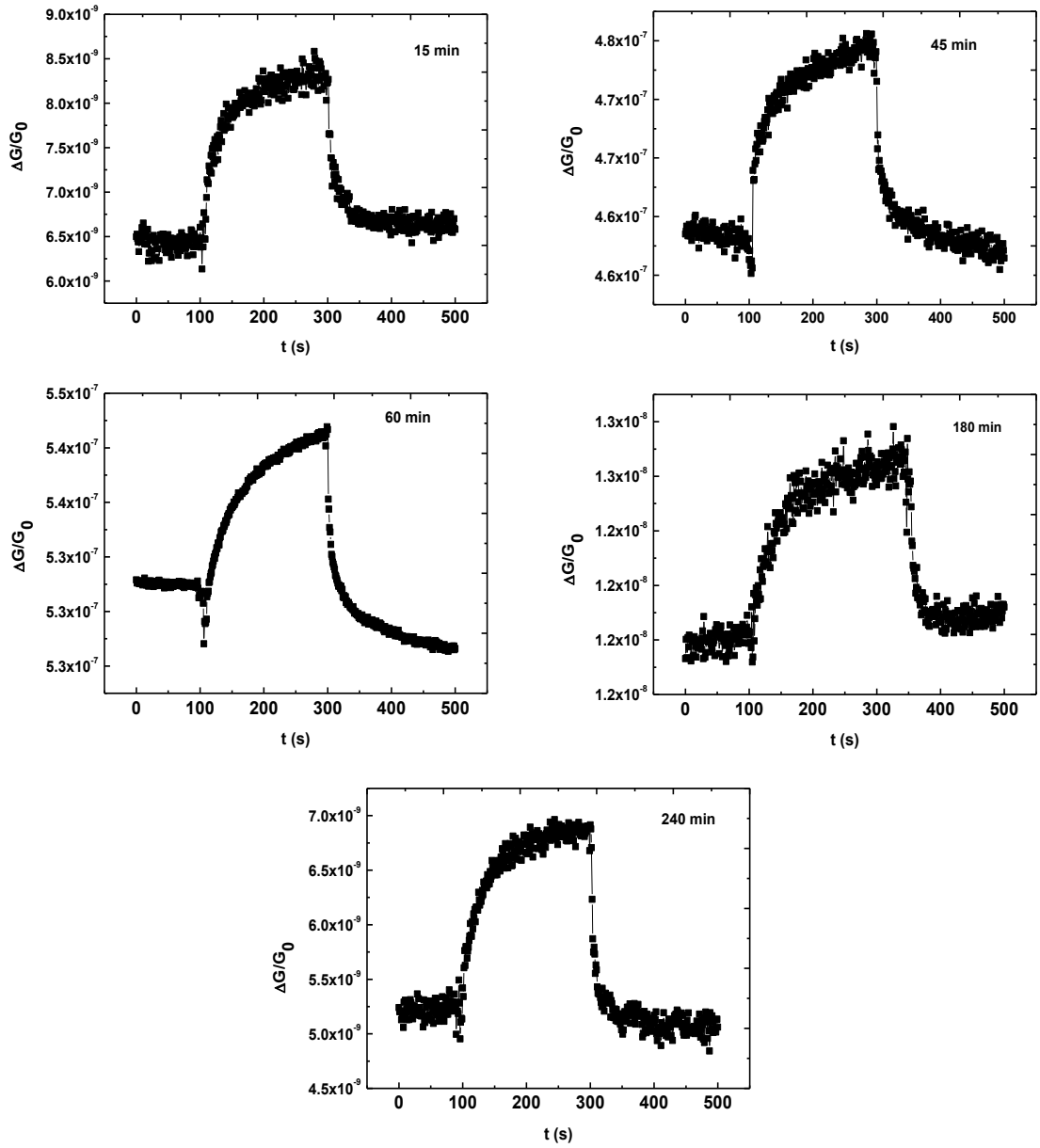

Figure 14. Response and recovery curves for OLA/WS_2 exposed to 240 ppm of NH_3 in ambient atmosphere.

3.3.5. Gas sensing mechanism

The gas sensing mechanism for semiconducting TMDCs is generally based on the transfer of an electric charge between the target analyte and the active material; thus, causing changes in the electrical properties of the sensing material. In this case, the NH_3 lone pair electron is transferred to the OLA/WS_2 sensor conduction band upon adsorption. Based on theoretical calculations, the analyte is physically adsorbed on the surface of a perfect 2D monolayer [38]. However, defects were introduced during colloidal synthesis of OLA/WS_2 nanostructures providing more reactive sites than the perfect lattice. Thus, increasing the chances of chemical adsorption between the analyte and active material. The observed increase in NH_3 sensitivity in the presence of humidity could be attributed to the increased acidity caused by the water molecules on the surface of the OLA/WS_2 sensor. Such increase can be explained by the hydroxylation reaction below:

Preprints (www.preprints.org) | NOT PEER-REVIEWED | Posted: 6 August 2020 doi:10.20944/preprints202008.0150.v1

$$SO_4^{2-}(OLA/WS_2\ surface) + H_2O \Longleftrightarrow H^+ + SO_4^{2-} + OH^- \quad (7)$$

Then, the basic NH_3 molecules donate more electrons to the acidic surface of the OLA/WS_2 sensor resulting in an increase in sensitivity.

XRD, Raman and SEM results suggested the existence of a bi-layer or few-layered OLA/WS_2. Based on these observations, the case of slow recovery at RT by OLA/WS_2 sensors can be explained by chemisorption which has been reported in previous studies for few-layered and bulk WS_2. It was argued that the NH_3 molecule can insert into the inner layers of WS_2 and interact with the two adjacent layers as shown in Figure 15 [2]. As a result, the NH_3 molecules between the layers of WS_2 nanosheets are much more difficult to desorb than the ones on the surface. This sensing mechanism is similar to the interaction process of NH_3 with layered TiS_2 and TaS_2; and in all these cases complete recovery was achieved by heating the sensors [35].

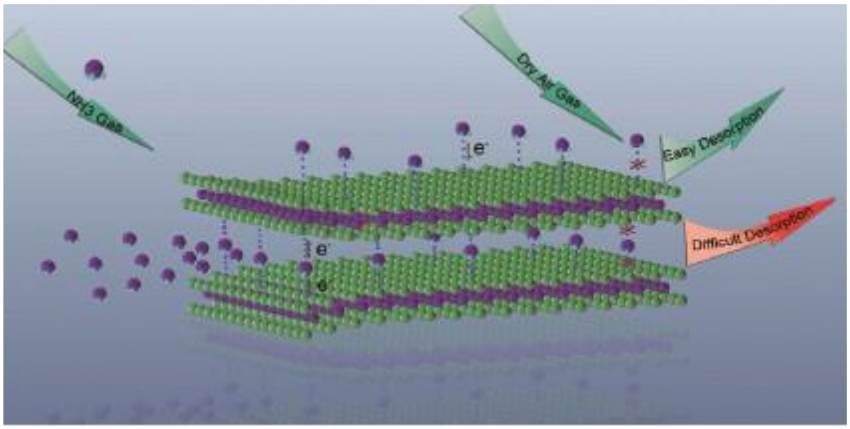

Figure 15. Schematic illustration of the interfacial interaction of NH_3 molecules with the surface and interlayer of WS_2 [2].

4. **Conclusions**

In summary, nanoflowers of OLA/WS_2 were successfully synthesized within 15 min via a relatively low temperature colloidal route. The nanoflower framework was broken down into its building blocks by simply increasing the incubation time. Partial oxidation did not adversely compromise the NH_3 sensing due to the presence of the capping agent, OLA. The sensors derived from nanoflowers presented higher response to NH_3 than the nanosheets. A very strong correlation between reaction time and the resultant morphology of the OLA/WS_2 nanostructures exists. The optical properties as shown can therefore be influenced by tuning the morphology of the nanostructures. This in turn can alter the sensing characteristics of a device and therefore impact its applicability in sensor technology. The 45 min derived sensor showed selectivity to NH_3 relative to acetone, ethanol, toluene and chloroform. Humidity interference was established and its significance was observed at very high % RH values. OLA/WS_2 sensors showed potential as NH_3 sensors at RT up to 75% RH. Evidence of incomplete recovery in both dry N_2 and RT conditions was demonstrated. These materials exhibited promising potential for use as active materials in RT resistive chemical sensors. Therefore, future work will focus on improving the recovery performance of the 45 min sensor by functionalizing the pristine OLA/WS_2 nanostructures with a noble metal, carbon nanomaterials, TMDC or MOS.

Supplementary Materials: The following are available online at www.mdpi.com/xxx/s1, Figure S1: Diagrams showing different colour changes during growth of OLA/WS_2 nanostructures, Figure S2: EDS analysis of the 180 min OLA/WS_2 nanostructures, Figure S3: FT-IR spectra of (a) pure OLA and (b) OLA/WS_2 synthesized in 45 min, Table S1: Raman intensity ratios and frequencies for the main phonon modes in OLA/WS_2, Table S2: UV and PL Raman intensity ratios and frequencies for the main phonon modes in OLA/WS_2, Table S3: Sensitivities of OLA/WS_2 based sensors to 1.5 µL of the NH_3, Table S4: Specificity of OLA/WS_2 based sensor (45 min) to 1.5 µL analytes.

Author Contributions: S.G., N.M., R.R. and I.H. conceptualized the experiments. S.G., S.M. Z.N. and R.R. performed the experiments. S.G. and R.R. analyzed the data. S.G. and R.R. prepared the original draft. The review and editing of the manuscript was done by S.G., R.R., M.A., I.H. and N.M. N.M. and I.H. supervised the research project. All authors have read and agreed to the published version of the manuscript.

Funding: This research was funded by the National Research Foundation, (TTK180419322895), the University of the Witwatersrand and the Department of Higher Education.

Acknowledgments: Department of Physics, Universidade Federal do Paranà, Brazil for technical support and materials used for experiments.

Conflicts of Interest: The authors declare no conflicts of interest.

References

1. Zhang, D.; Wu, J.; Li, P.; Cao, Y.; Yang. Z. Hierarchical Nanoheterostructures of Tungsten Disulfide Nanoflowers Doped with Zinc Oxide Hollow Spheres: Benzene Gas Sensing Properties and First Principles Study. *ACS Appl. Mater. Interfaces* **2019**, 11, 31245-31256. DOI.10.1021/acsami.9b07021.
2. Ouyang, C.; Chen, Y.; Qin, Z.; Zeng, D.; Zhang, J.; Wang, H.; Xi, C. Two-dimensional WS2-based nanosheets modified by Pt quantum dots for enhanced room-temperature NH_3 sensing properties. *Appl. Surf. Science* **2018**, 455, 45. https://doi.org/10.1016/j.apsusc.2018.05.148.
3. Ko, K. Y.; Song. J-G.; Kim, Y.; Choi, T.; Shin, S.; Lee, C. W.; Lee, K.; Koo, J.; Lee, H.; Kim, J.; Lee, T.; Park, J.; Kim, H. Improvement of Gas -Sensing Performance of Large-Area Tungstedn Disulfide Nanosheets by Surface Functionalization. *ACS Nano* **2016**, 10, 9287-9296. DOI.10.1021/acsnano.6b03631.
4. Perrozzi, F.; Emamjomeh, S.M.; Paolucci, V.; Taglier, G.; Ottaviano, L.; Cantalini, C. Thermal Stability of WS_2 Flakes and Gas Sensing Properties of WS_2/WO_3 Composite to H_2, NH_3 and NO_2. *Sens. Actuators B: Chemical* **2017**, 243, 812-822. http://dx.doi.org/10.1016/j.snb.2016.12.069.
5. Chen, Y.; Pei, Y.; Jiang, Z.; Shi, Z.; Xu, J.; Wu, D.; Xu, T.; Tian, Y.; Wang, X.; Li, X. Humidity Sensing Properties of the Hydrothermally Synthesized WS_2-modified SnO_2 Hybrid Nanocomposite. *Appl. Surf. Science* **2018**, 447, 325-330. https://doi.org/10.1016/j.apsusc.2018.03.154.
6. Asres, G.A.; Baldoví, J.J.; Dombovari, A.; Järvinen, T.; Lorite, G.S.; Mohl, M.; Shchukarev, A.; Paz, A.P.; Xian, L.; Mikkola, J-P.; Spetz, A.L.; Jantunen, A.; Rubio, Á.; Kordas, K. Ultrasensitive H_2S Gas Sensors Based on p-Type WS_2 Hybrid Materials. *Nano Res.* **2018**, 11(8), 4215-4224. https://doi.org/10.1007/s12274-018-2009-9.
7. Huo, N.; Yang, S.; Wei, Z.; Li, S-S.; Xia, J-B.; Li, J. Photoresponsive and Gas Sensing Field-Effect Transistors based on Multilayer WS_2 Nanoflakes. *Sci. Rep*. **2014**, 4, 5209. DOI:10.1038/srep05209.
8. Airo, M.A.; Rodrigues, R.; Gqoba, S.; Ntholeng, N.; Otieno, F.; Moloto, M.J.; Greenshields, M.W.C.C.; Hummelgen, I.A.; Moloto, N. Colloidal InSe Nanostructures: Effect of Morphology on their Chemical Sensitivity to Methanol and Formaldehyde Fumes. *Sens. Actuators B: Chemical* **2016**, 236, 116-125. https://doi.org/10.1016/j.snb.2016.05.15.
9. Xaba, T.; Moloto, M.J.; Moloto, N. The Effect of Water-soluble Capping Molecules in the "Green" Synthesis of CdS Nanoparticles Using the (Z)-2-(pyrrolidin-2-ylidene)thiourea Ligand. *Mater. Lett.* **2015**, 146, 91- 95. https://doi.org/10.1016/j.matlet.2015.01.153.
10. Moloto, N.; Moloto, M.J.; Moloto, N.J.; Ray, S.S. Synthesis and Characterization of Nickel Selenide Nanoparticles: Size and Shape Determining Parameters. *J. Cryst. Growth* **2011**, 324 (1), 41. https://doi.org/10.1016/j.jcrysgro.2011.03.047.
11. Yuan, Z.; Li, R.; Meng, F.; Zhang, J.; Zuo, K.; Han, E. Approaches to Enhancing Gas Sensing Properties: A Review. *Sensors* **2019**, 19 (1495), 1-25. doi: 10.3390/s19071495.

12. Luo, Y-K.; Song, F.; Wang, X-L; Wang, Y-Z. Pure Copper Phosphate Nanostructures with Controlled Growth: A Versatile Support for Enzyme Immobilization. *Cryst. Eng. Comm.* **2017**, 19, 2996-3002. DOI: 10.1039/C7CE00466D.
13. Wu, Y.-c.; Liu, Z.-m; Chen, J-t.; Cai, X-j.; Na, P. Hydrothermal Fabrication of Hyacinth Flower-like Nanorods and their Photocatalytic Properties. *Mater. Lett.* **2017**, 189, 282-285. https://doi.org/10.1016/j.matlet.2016.11.024.
14. Li, X.; Zhang, J.; Liu, Z.; Fu, C.; Niu, C. WS_2 Nanoflowers on Carbon Nanotube Vines with Enhanced Electrochemical Performances for lithium and sodium-ion batteries. *J. Alloys Compd.* **2018**, 766, 656-662. https://doi.org/10.1016/j.jallcom.2018.07.008.
15. Nguyen, T.P.; Kim, S.Y.; Lee, T.H.; Jang, H.W.; Van Led, Q.; Kim, I.T. Facile Synthesis of W_2C@WS_2 Alloy Nanoflowers and their Hydrogen Generation Performance. *Appl. Surf. Science* **2020**, 504 (144389). https://doi.org/10.1016/j.apsusc.2019.144389.
16. Magdassi, S.; Grouchko, M.; Kamyshny, A. Copper Nanoparticles for Printed Electronics: Routes Towards Achieving Oxidation Stability. *Materials* **2010**, **3** (9), 4626-4638. doi: 10.3390/ma3094626.
17. Li, X.; Li, X.; Li, X.; Wang, J.; Zhang, Z. WS_2 Nanoflakes Based Selective Ammonia Sensors at Room Temperature. *Sens. Actuators B: Chem* **2017**, 240, 273. http://dx.doi.org/10.1016/j.snb.2016.08.163.
18. Greenspan, L. *J. Res. Natl. Bur. Stand.* Humidity Fixed Points of Binary Saturated Aqueous Solutions. **1977**, 81 A (1), 89-96.
19. Feng, C.; Huang, L.; Guo, Z.; Liu, H. Synthesis of tungsten disulfide (WS_2) nanoflakes for lithium ion battery application. *Electrochem. Commun.* **2007**, 9, 119. https://doi.org/10.1016/j.elecom.2006.08.048.
20. Varghese, S.S.; Varghese, S.H.; Swaminathan, S.; Singh, K.K.; Mittal, V. Two-Dimensional Materials for Sensing: Graphene and Beyond. *Electronics* **2015**, 4, 651- 687. https://doi.org/10.3390/electronics4030651.
21. Tan, H.; Fan, Y.; Zhou, Y.; Chen, Q.; Xu, W.; Warner, J.H. Ultrathin 2D Photodetectors Utilizing Chemical Vapor Deposition Grown WS_2 with Graphene Electrodes. *ACS Nano* **2016**, 10, 7866−7873. https://doi.org/10.1021/acsnano.6b03722.
22. Berkdemir, A.; Gutierrez, H.R.; Botello-Mendez, A.R.; Perea-Lopez, N.; Elıas, A.L.; Chia, C-I.; Wang, B.; Crespi, V.H.; Lopez-Urıas, F.; Charlier, J-C.; Terrones, H.; Terrones, M. Identification of Individual and Few Layers of WS_2 Using Raman Spectroscopy. *Sci. Rep.* **2013**, 3 (1755). DOI:10.1038/srep01755.
23. Chiu, S-W.; Tang, K-T. Towards a Chemiresistive Sensor-Integrated Electronic Nose: A Review. *Sensors* **2013**, 13, 14214 -14247. https://doi.org/10.3390/s131014214.
24. Atewologun, A.; Ge, W.; Stiff-Roberts, A.D. Characterization of Colloidal Quantum Dot Ligand Exchange by X-ray Photoelectron Spectroscopy. *J. Electron. Mater.* **2013**, 42 (5), 809-814. DOI: 10.1007/s11664-012-2371-4.
25. Liu, I-S.; Lo, H-H.; Chien, C-T.; Lin, Y-Y.; Chen, C-W.; Chan, Y-F.; Sue, W-F.; Liou, S-C. Enhancing Photoluminescence Quenching and Photoelectric Properties of CdSe Quantum Dots with Hole Accepting Ligands. *J. Mater. Chem.*, **2008**, 18, 675. DOI: 10.1039/B715253A.
26. Cao, S.; Zhao, C.; Peng, L. The 3D WS_2 Microspheres: Preparation, Characterization and Optical Absorption Properties. *Mater. Lett.* **2016**, 164, 452-455. https://doi.org/10.1016/j.matlet.2015.11.012.
27. Pagona, G.; Bittencourt,C.; Arenal, R.; Tagmatarchis, N. Exfoliated Semiconducting Pure 2H-MoS_2 and 2H-WS_2 Assisted by Chlorosulfonic Acid. *Chem. Commun*. **2015**, 51, 12950-12953. DOI: 10.1039/c5cc04689k.
28. Zhao, W.; Ghorannevis, Z.; Chu, L.; Toh, M.; Kloc, C.; Tan, P-H.; Eda, G. Evolution of Electronic Structure in Atomically Thin Sheets of WS_2 and WSe_2. *ACS Nano* **2013**, **7** (1), 791. 10.1021/nn305275h.
29. Gutiérrez, H.R.; Perea-López, N.; Elías, A.L.; Berkdemir, A.; Wang, B.; Lv, R.; López-Urías, F.; Crespi, V.H.; Terrones, H.; Terrones. M. Extraordinary Room-Temperature Photoluminescence in Triangular WS_2 Monolayers *Nano Lett*. **2013**, 13, 3447- 3454. https://doi.org/10.1021/nl3026357.
30. Kim, T.H.; Kim, Y.H.; Park, S. Y.; Kim, S.Y.; Jang, H. W. Two-Dimensional Transition Metal Disulfides for Chemoresistive Gas Sensing: Perspective and Challenge. *Chemosensors* **2017**, 5 (15), 1-19. https://doi.org/10.3390/chemosensors5020015.
31. Wang, X.; Gu, D.; Li, X.; Lin, S.; Zhao, S.; Rumyantseva, M.N.; Gaskov, A.M. Reduced Graphene Oxide Hybridized with WS_2 Nanoflakes based Heterojunctions for Selective Ammonia Sensors at Room Temperature. *Sens. Actuators B: Chemical* **2019**, 282, 290-299. https://doi.org/10.1016/j.snb.2018.11.080.
32. Lee, J-H. Gas Sensors Using Hierarchical and Hollow Oxide Nanostructures: Overview. *Sens. Actuators B: Chemical* **2009**, 140 (1), 319- 336. doi:10.1016/j.snb.2009.04.026.

33. Li, Y-X.; Guo, Z.; Su, Y.; Jin, X-B.; Tang, X-H.; Huang, J-R.; Huang, X-J.; Li, M-Q.; Liu, J-H. Hierarchical Morphology-Dependent Gas-Sensing Performances of Three-Dimensional SnO_2 Nanostructures *ACS Sens*. **2017**, 2, 102-110. DOI:10.1021/acssensors.6b00597.
34. Llobet, E.; Molas, G.; Molinàs, P.; Calderer, J.; Vilanova, X.; Brezmes, J.; Sueiras, J.E.; Correiga, X. Fabrication of Highly Selective Tungsten Oxide Ammonia Sensors. *J. Electrochem. Soc.* **2000**, 147 (2) 776- 779 (2000).
35. Qin, Z.; Zeng, D.; Zhang, J.; Wu, C.; Wen, Y.; Shan, B.; Xie, C. Effect of Layer Number on Recovery Rate of WS_2 Nanosheets for Ammonia Detection at Room Temperature. *Appl. Surf. Sci.* **2017**, 414, 244 -250. https://doi.org/10.1016/j.apsusc.2017.04.063.
36. Late, D.J.; Huang, Y-K.; Liu, B.; Acharya, J.; Shirodkar, S.N.; Luo, J.; Yan, A.; Charles, D.; Waghmare, U.V.; Dravid, V.P.; Rao, C.N.R. Sensing behavior of atomically thin-layered MoS_2 transistors. *ACS Nano* **2013**, 7 (6), 4879-91. doi: 10.1021/nn400026u.
37. Marr, I.; Groß, A.; Moos, R. Overview on Conductometric Solid-state Gas Dosimeters. *J. Sens. Sens. Syst.* **2014**, 3, 29-46. doi:10.5194/jsss-3-29-2014.
38. Zeng, Y.; Lin, S.; Gu, D.; Li, X. Two-Dimensional Nanomaterials for Gas Sensing Applications: The Role of Theoretical Calculations. *Nanomaterials* **2018**, 8 (851), 1-16. https://doi.org/10.3390/nano8100851.